

# Curvature dependent surface tension from a simulation of a cavity in a Lennard-Jones liquid close to coexistence

M. P. Moody and P. Attard

*Ian Wark Research Institute, University of South Australia, Mawson Lakes, South Australia 5095*

(Received 17 July 2001; accepted 4 September 2001)

Monte Carlo simulations have been used to calculate the surface tension of a planar liquid-vapor interface of a Lennard-Jones fluid using a new cylindrical truncation correction procedure. A bubble was mimicked by simulating a Lennard-Jones liquid close to coexistence containing a single immobile hard-sphere cavity. From the density profile of this system the curvature dependent surface tension has been estimated via calculation of the Helmholtz free energy of the system and separately using a large cavity contact density expansion. Evidence is presented that the Tolman length becomes increasingly negative as the critical temperature is approached and possibly changes sign. © 2001 American Institute of Physics. [DOI: 10.1063/1.1413514]

## I. INTRODUCTION

The dependence of surface tension on radius of curvature is fundamental to the study of the properties of small droplets and bubbles. In 1949, using Gibbs' theory of capillarity, Tolman<sup>1</sup> gave a simple expression for the surface tension of a curved interface,  $\gamma(R)$ ,

$$\gamma(R) = \gamma_\infty \left( 1 - \frac{2\delta}{R} \right), \quad (1.1)$$

where  $\gamma_\infty$  is the value of the surface tension for a planar liquid-vapor interface. To leading order,  $R$  is any measure of the radius of the interface and  $\delta$  is the Tolman length. The Tolman length may be shown to equal the distance between the equimolar dividing surface,  $R_e$ , and the surface of tension,  $R_s$ , in the planar limit,<sup>2</sup>

$$\delta = \lim_{R_e, R_s \rightarrow \infty} R_e - R_s. \quad (1.2)$$

The Tolman length encompasses the primary curvature correction to the planar surface tension.

Tolman believed that the value of the surface tension of small droplets and bubbles would be less than the planar value, which implies that  $\delta$  would be positive and small. However, the magnitude and even sign of the Tolman length, and its dependence on temperature and droplet size still remains uncertain. Equation (1.2) implies that the Tolman length is of molecular size and therefore significant deviation from the planar value of the surface tension would only be seen in bubbles or droplets of sub-microscopic dimensions. Such molecular scales have posed almost insurmountable practical challenges, which have severely limited the volume of experimental results.<sup>3</sup> The bulk of work concerning  $\gamma(R)$  and the size of  $\delta$  has come from theoretical consideration. Recent studies have included computer simulations, theoretical thermodynamic derivation and density functional theory.

Molecular dynamics computer simulations of Lennard-Jones fluids have been used by several authors to study this phenomenon, including work by Nijmeijer *et al.*,<sup>4</sup> Haye and Bruin<sup>5</sup> and El Bardouni *et al.*<sup>6</sup> Nijmeijer *et al.* obtained a

pressure tensor expression for the Tolman length from thermodynamic analysis of the pressure difference across the interface of a liquid drop in coexistence with its own vapor. By studying the pressure drop across the interface of droplets in simulations, they found  $|\delta| < 0.7 \sigma$ , where  $\sigma$  is the molecular diameter, but could not be definite about its sign. Haye and Bruin, using molecular dynamics simulations of a planar liquid-vapor interface, estimated the Tolman length from a relation that expressed it as an integral over the pair distribution function of the planar interface.<sup>7</sup> They concluded that  $\delta$  was small ( $\sim 0.2 \sigma$ ) and positive for all temperatures. El Bardouni *et al.* evaluated the pressure profiles across a liquid-vapor interface using molecular dynamics simulations. Within the noise of their simulation, comparing planes with drops of the order of  $R = 10 \sigma$ , they found the surface tension to be curvature independent. They did, however, find that the position of the surface of tension was less than the equimolar surface for spheres for all temperatures, which implies a Tolman length of the order of  $0.5 \sigma$ .

Giessen, Blokhuis, and Bukman<sup>8</sup> applied rigorous theoretical thermodynamic consideration to the problem. They presented expressions for the surface tension and Tolman length in mean-field approximation. The numerically calculated values of  $\delta$  were found to be negative and close to  $0.2 \sigma$  in magnitude. The Fisher droplet model was used by Kalikmanov<sup>9</sup> to formulate a semiphenomenological theory of the Tolman length. This model gave a positive Tolman length, close to  $0.2 \sigma$ , away from the critical temperature,  $T_c$ . However, approaching  $T_c$  it changed sign and diverged. Bykov and Zeng<sup>10</sup> developed an approach to derive analytical results in the framework of density functional theory. A patching model for the density profiles was based on analytical expressions for the asymptote of the profiles which can be used in the statistical mechanics formulas for  $\gamma(R)$  and  $\delta$ . They found the Tolman length to be small, negative and weakly dependent on  $T$ .

This work uses Monte Carlo simulations to obtain the surface tension of both planar and curved interfaces of a Lennard-Jones (12-6) fluid. In Sec. II we examine the planar

interfacial value of the surface tension at liquid-vapor coexistence. A new cylindrical truncation correction to the surface tension has been derived and results are presented for several temperatures between the triple point and  $T_c$ . Density profiles are also given.

In Sec. III we present results for a hard-sphere cavity in a liquid close to coexistence, including the derivation of a spherical truncation correction technique. We present evidence that such a cavity is a reasonable qualitative model of the liquid-vapor interface, and that the results are applicable to gas bubbles. Previous work in this area includes molecular dynamics simulations by Stecki and Toxvaerd.<sup>11</sup> They studied systems containing a cavity with radii ranging from  $0.5\sigma$  to a hard wall at a single temperature. They measured the density profile, the density at the surface of the cavity and extracted the chemical potential of the cavity. Samborski *et al.*,<sup>12</sup> using a weighted density approximation further investigated this area and found qualitative agreement with the previous computer simulations. Poniewierski and Stecki<sup>13</sup> theoretically derived formal expressions for the surface tension of a fluid in contact with a hard spherical wall and proposed a method for expansion in powers of curvature and applied it to the first correction. Henderson<sup>14</sup> studied the behavior of fluids at hard walls. He obtained a formula expressing the curvature dependent surface tension as a function of the derivative of the density of a liquid at the surface of a cavity with respect to its radius. The simulation of a cavity in a liquid provides the advantage of a simpler system with a known and unambiguous surface at all times. We present radially dependent density profiles for systems with a single immobile cavity, whose radii ranges from  $.1\sigma$  to  $3.5\sigma$ , at three temperatures and use them to test a small cavity theory and the Percus-Yevick integral equation approximation. The surface tension is calculated from the Helmholtz free energy of the system.<sup>15</sup>

## II. PLANAR GEOMETRY

### A. Potential energy tail correction

The Monte Carlo technique of Metropolis was used to simulate a liquid film in equilibrium with its vapor phase in a rectangular box of dimensions  $L_{xy} \times L_{xy} \times L_z$ . The number of atoms,  $N$ , was chosen to be large enough such that the formation of the liquid as a planar slab was always favorable. Periodic boundary conditions were imposed along the x and y axes and an external potential was introduced perpendicular to the free surfaces of the liquid at  $z = -L_z/2$ , and  $z = L_z/2$  following Lee *et al.*<sup>16</sup> This external potential prevents indefinite evaporation of particles from the liquid. In addition a trial movement in which a molecule crossed the  $z$  plane was immediately rejected, preventing excessive translational motion of the center-of-mass of the liquid film, which might otherwise have affected analysis of the interfacial region.<sup>16</sup> This effectively pinned the liquid to the center of the box. The vapor phase was made sufficiently large so that the external potential made no contribution to the surface tension. The liquid was held together solely by its own cohesion.

Molecules in the box interacted with each other via the 12-6 Lennard-Jones potential,

$$u_{\text{LJ}}(r_{ij}) = 4\epsilon \left[ \left( \frac{\sigma}{r_{ij}} \right)^{12} - \left( \frac{\sigma}{r_{ij}} \right)^6 \right], \quad (2.1)$$

and with the external potential at the  $z$ -ends of the box by

$$u_{\text{ext}}(z_i) = \begin{cases} 0, & |z_i| < \left| \frac{L_z}{2} - 2\sigma \right| \\ 12\epsilon \left( \frac{1}{\left( \frac{L_z}{2\sigma} - |z_i/\sigma| \right)^2 - 0.25} \right), & |z_i| \geq \left| \frac{L_z}{2} - 2\sigma \right| \\ \infty, & |z_i| > \left| \frac{L_z}{2} \right| \end{cases}, \quad (2.2)$$

where  $\epsilon$  is the potential well depth of the Lennard-Jones potential and  $\sigma$  is the collision parameter. For simulated Argon<sup>16</sup>  $\epsilon/k = 119.4$  K and  $\sigma = 0.34$  nm.

In keeping with the symmetry of the inhomogeneous system a cylindrical truncation of the Lennard-Jones potential at long range was employed,<sup>17</sup> as opposed to the more conventional spherical cutoff used for simulations of bulk systems. The truncated potential was

$$u_{\text{LJ}}^c(s_{ij}, z_{ij}) = \begin{cases} u_{\text{LJ}}(\sqrt{s_{ij}^2 + z_{ij}^2}), & s_{ij} < s_c \text{ and } z_{ij} < z_c \\ 0, & s_{ij} > s_c \text{ or } z_{ij} > z_c \end{cases}, \quad (2.3)$$

where  $s_{ij} = \sqrt{(x_i - x_j)^2 + (y_i - y_j)^2}$  and  $z_{ij} = z_i - z_j$ . In view of the periodic boundary conditions the cylindrical cutoff radius was always  $s_c < L_{xy}/2$  and the nearest neighbor convention was implemented. A tail correction was implemented by defining the tail potential as

$$u_{\text{tail}}(r_{ij}) = u_{\text{LJ}}(r_{ij}) - u_{\text{LJ}}^c(r_{ij}). \quad (2.4)$$

The total configurational energy of the system is given by

$$U_{\text{LJ}} = \left\langle \frac{1}{2} \sum_i^N \sum_{j \neq i}^N u_{\text{LJ}}^c(s_{ij}, z_{ij}) \right\rangle + U_C, \quad (2.5)$$

where the angular brackets denote a canonical ensemble average. The tail correction can be derived from the expression for the total energy in terms of the pair density,

$$U_{\text{LJ}} = \frac{1}{2} \int d\vec{r}_1 d\vec{r}_2 \rho^{(2)}(\vec{r}_1, \vec{r}_2) u_{\text{LJ}}(|\vec{r}_1 - \vec{r}_2|), \quad (2.6)$$

if we assume that the density of the system is independent of both its x and y coordinates so that

$$\rho^{(2)}(\vec{r}_1, \vec{r}_2) = \rho(z_1)\rho(z_2)g(z_1, z_2, s_{12}). \quad (2.7)$$

For the tail, correction particles are far apart, so that the radial distribution function is unity,  $g(z_1, z_2, s_{12}) \sim 1$  and  $\rho^{(2)}(\vec{r}_1, \vec{r}_2) \sim \rho(z_1)\rho(z_2)$ . Hence

$$U_C = \frac{1}{2} L_{xy}^2 \int_{-L_z/2}^{L_z/2} dz_1 \rho(z_1) \int_{-L_z/2}^{L_z/2} dz_2 \rho(z_2) \times \int d\vec{s}_{12} u_{\text{tail}}(s_{12}, z_{12}). \quad (2.8)$$

Using the fact that at long range,  $u_{LJ}(r_{12}) \sim -4\varepsilon(\sigma/r_{12})^6$ , one obtains

$$\int d\vec{s}_{12} u_{\text{tail}}(s_{12}, z_{12}) = -2\pi \int_{s_c}^{\infty} ds_{12} s_{12}^4 \varepsilon \left( \frac{\sigma}{\sqrt{s_{12}^2 + z_{12}^2}} \right)^6 = \frac{-2\pi\varepsilon\sigma^6}{(s_c^2 + z_{12}^2)^2}. \quad (2.9)$$

The long range correction is then given by

$$U_C = \frac{1}{2} L_{xy}^2 \int_{-L_z/2}^{L_z/2} dz_1 \rho(z_1) \left[ \int_{z_<}^{z_>} dz_2 \rho(z_2) \int_{s_c}^{\infty} u(r_{12}) d\vec{s}_{12} + \int_{z_>}^{L_z/2} dz_2 \rho(z_2) \int_0^{\infty} u(r_{12}) d\vec{s}_{12} + \int_{-L_z/2}^{z_<} dz_2 \rho(z_2) \int_0^{\infty} u(r_{12}) d\vec{s}_{12} \right], \quad (2.10)$$

where  $z_> = \text{Min}[(z_1 + z_c), L_z/2]$  and  $z_< = \text{Max}[(z_1 - z_c), -L_z/2]$ .

Substituting into Eq. (2.9) into Eq. (2.10) one has

$$U_C = -\frac{1}{2} L_{xy}^2 \int_{-L_z/2}^{L_z/2} dz_1 \rho(z_1) \left[ \int_{z_<}^{z_>} dz_2 \frac{2\pi\varepsilon\sigma^6\rho(z_2)}{(s_c^2 + z_{12}^2)^2} + \int_{z_>}^{L_z/2} dz_2 \frac{2\pi\varepsilon\sigma^6\rho(z_2)}{z_{12}^4} + \int_{-L_z/2}^{z_<} dz_2 \frac{2\pi\varepsilon\sigma^6\rho(z_2)}{z_{12}^4} \right]. \quad (2.11)$$

Equation (2.11) was evaluated during the simulation by numerical integration using the average density profile,  $\rho(z)$ . The value of the latter was obtained by dividing the simulation volume into a series of cells of width  $\Delta_z$  along the  $z$ -axis, where  $\Delta_z$  is small enough to assume constant density within the cell. A histogram of the number of atoms in each cell was constructed to estimate the average number of atoms in the  $i$ th cell. The density was given by

$$\rho(z(i)) = \frac{\bar{h}(i)}{\Delta_z L_{xy}}, \quad (2.12)$$

where  $z(i) = -L_z/2 + \Delta_z/2 + (i-1)\Delta_z$ , and  $\bar{h}(i)$  is the average number of particles in the  $i$ th cell.

The truncation correction procedure was also implemented for the calculation of the change in the total energy of the system due to the trial movement of a single atom. This correction may become significant in terms of whether a move is accepted or rejected in the Metropolis method and thus to the overall chain of states sampled during the simulation. The change in energy produced by a single trial movement of atom  $i$ ,  $r_i \rightarrow r'_i$  is given by

$$\Delta U = \sum_{j \neq i}^N u(r'_{ij}) + u_{\text{ext}}(z'_i) + T(z'_i) - \sum_{j \neq i}^N u(r_{ij}) - u_{\text{ext}}(z_i) - T(z_i). \quad (2.13)$$

The correction  $T$  is taken from the bracketed part of Eq. (2.11)

$$T(z_1) = - \int_{z_<}^{z_>} dz_2 \frac{2\pi\varepsilon\sigma^6\rho(z_2)}{(s_c^2 + z_{12}^2)^2} - \int_{z_>}^{L_z/2} dz_2 \frac{2\pi\varepsilon\sigma^6\rho(z_2)}{z_{12}^4} - \int_{-L_z/2}^{z_<} dz_2 \frac{2\pi\varepsilon\sigma^6\rho(z_2)}{z_{12}^4}. \quad (2.14)$$

## B. Planar surface tension

The surface tension and the pressure were calculated in the simulation by means of the virial expressions<sup>2</sup>

$$\gamma = \frac{1}{L_{xy}^2} \left\langle \sum_{i < j}^N \frac{(x_i - x_j)^2 + (y_i - y_j)^2 - 2(z_i - z_j)^2}{2r_{ij}} u'(r_{ij}) \right\rangle \quad (2.15)$$

and

$$P = \frac{NkT}{L_z L_{xy}^2} - \frac{1}{L_z L_{xy}^2} \left\langle \sum_{i < j}^N \frac{(z_i - z_j)^2}{r_{ij}} u'(r_{ij}) \right\rangle. \quad (2.16)$$

Like the energy the surface tension is corrected for cylindrical truncation of the potential by writing Eq. (2.15) in terms of the pair density

$$\gamma = \frac{1}{2L^2} \int_V d\vec{r}_1 d\vec{r}_2 \rho^{(2)}(\vec{r}_1, \vec{r}_2) \Gamma(\vec{r}_{12}), \quad (2.17)$$

where

$$\Gamma(r_{ij}) = \frac{(x_i - x_j)^2 + (y_i - y_j)^2 - 2(z_i - z_j)^2}{2r_{ij}} u'(r_{ij}). \quad (2.18)$$

Again assuming that the singlet density is independent of its  $x$  and  $y$  coordinates and that  $g(z_1, z_2, s_{12}) = 1$ , this may be written as

$$\gamma = \frac{1}{2L^2} \int_{-L_z/2}^{L_z/2} dz_1 \int_{-L_z/2}^{L_z/2} dz_2 \int_{L^2} ds_1 \times \int_{L^2} d\vec{s}_{12} \rho(z_1) \rho(z_2) \Gamma(s_{12}, z_{12}). \quad (2.19)$$

The surface tension tail correction is given by

$$\gamma_{\text{tail}} = \frac{1}{2} \int_{-L_z/2}^{L_z/2} dz_1 \rho(z_1) \times \left[ \int_{z_<}^{z_>} dz_2 \rho(z_2) \int_{s_{12} > s_c} ds_{12} \frac{u'(r_{12})}{r_{12}} \left( \frac{s_{12}^2 - 2z_{12}^2}{2} \right) + \int_{z_>}^{L_z/2} dz_2 \rho(z_2) \int_0^{\infty} ds_{12} \frac{u'(r_{12})}{r_{12}} \left( \frac{s_{12}^2 - 2z_{12}^2}{2} \right) + \int_{-L_z/2}^{z_<} dz_2 \rho(z_2) \int_0^{\infty} ds_{12} \frac{u'(r_{12})}{r_{12}} \left( \frac{s_{12}^2 - 2z_{12}^2}{2} \right) \right]. \quad (2.20)$$

Equation (2.20) can be evaluated using the asymptote,  $u_{LJ}(r_{12}) \sim -4\varepsilon(\sigma/r_{12})^6$

$$\begin{aligned}
\gamma_{\text{tail}} = & \frac{1}{2} \int_{-L_z/2}^{L_z/2} dz_1 \left[ 4\pi\epsilon\sigma^6 \int_{z_<}^{z_>} dz_2 \rho(z_2) \right. \\
& \times \left( \frac{s_c^2}{(s_c^2 + z_{12}^2)^3} + \frac{1}{2(s_c^2 + z_{12}^2)^2} - \frac{2z_{12}^2}{(s_c^2 + z_{12}^2)^3} \right) \\
& - 6\pi\epsilon\sigma^6 \int_{z_>}^{L_z/2} dz_2 \rho(z_2) \frac{1}{z_{12}^4} \\
& \left. - 6\pi\epsilon\sigma^6 \int_{-L_z/2}^{z_<} dz_2 \rho(z_2) \frac{1}{z_{12}^4} \right]. \quad (2.21)
\end{aligned}$$

An expression for the virial pressure truncation correction was similarly derived

$$\begin{aligned}
P_{\text{tail}} = & -\frac{1}{2} \int_{-L_z/2}^{L_z/2} dz_1 \left[ \frac{4\pi\epsilon\sigma^6}{L_z} \left( \int_{z_>}^{z_>} dz_2 \rho(z_2) \frac{z_{12}^2}{(s_c^2 + z_{12}^2)^3} \right. \right. \\
& \left. \left. + \int_{z_>}^{L_z/2} dz_2 \rho(z_2) \frac{1}{z_{12}^4} + \int_{-L_z/2}^{z_<} dz_2 \rho(z_2) \frac{1}{z_{12}^4} \right) \right]. \quad (2.22)
\end{aligned}$$

### C. Planar results

From an initial lattice configuration, 30 000 cycles were taken to equilibrate the system. Statistical measurements were made in the following 150 000 cycles. A cycle was defined as a trial move of every atom in the system. After equilibration, the simulation was divided up into approximately 50 blocks of 30 000 cycles, during which statistical measurements were made. An average over each block was taken for the surface tension, pressure, and potential energy. At the end of the simulation an average over these blocks was taken, and the statistical error was estimated from the fluctuations in the block averages. Simulations were carried out at six different temperatures. In general  $z_c^* = 3.5$ ,  $s_c^* = 3.5$ , but at three temperatures several different cutoff scenarios were investigated. The system contained 568 atoms, the length of the box in the x and y directions were fixed at  $L_{xy}^* = 9$ . However at higher temperatures the length in the z direction was increased to compensate for an increase in the width of the interface. The reduced temperature was defined as  $T^* = kT/\epsilon$ , the reduced length as  $z^* = z/\sigma$ , the reduced surface tension as  $\gamma^* = \gamma\sigma^2/\epsilon$ , and the reduced density as  $\rho^* = \rho\sigma^3$ .

The results for the corrected surface tension and the contribution from the tail correction are shown in Table I. The applied cylindrical truncation and correction proved to be an effective technique that minimized finite size effects over a wide range of temperatures from the triple point of Argon to near its critical temperature. The variations between the surface tensions simulated with different cutoff scenarios is less than the value of the tail corrections, and comparable to the statistical error. It is interesting to note that the correction in the surface tension to  $s_c$  is positive and the correction to  $z_c$  negative. This cancellation of truncation error means for the larger  $z_c$  and smaller  $s_c$  the total correction to the surface

TABLE I. Simulation results for surface tension and cylindrical truncation correction. The corrected surface tension,  $\gamma^* = \gamma^c + \gamma_{\text{tail}}$ , which is the sum of the truncated surface tension,  $\gamma^c$  and the tail correction,  $\gamma_{\text{tail}}$ . The standard error of the corrected surface tension is also given.

$T^*$	$L_z^*$	$s_c^*$	$z_c^*$	$\gamma^*$	$\gamma_{\text{tail}}^*$
0.70	20	3.5	3.5	1.152±0.023	0.309
0.70	20	3.5	4.5	1.156±0.020	0.43
0.70	20	4.5	3.5	1.169±0.018	0.041
0.70	20	4.5	4.5	1.154±0.018	0.168
0.80	22	3.5	3.5	0.916±0.019	0.280
0.90	26	3.5	3.5	0.697±0.016	0.242
1.00	26	3.5	3.5	0.505±0.018	0.205
1.00	26	3.5	4.5	0.538±0.012	0.316
1.00	26	4.5	3.5	0.519±0.012	-0.001
1.00	26	4.5	4.5	0.529±0.013	0.113
1.10	26	3.5	3.5	0.350±0.015	0.166
1.20	30	3.5	3.5	0.156±0.013	0.107
1.20	30	3.5	4.5	0.177±0.013	0.199
1.20	30	4.5	3.5	0.178±0.010	-0.033
1.20	30	4.5	4.5	0.176±0.013	0.062

tension is large, while a simulation with a smaller  $z_c$  and larger  $s_c$  returns a smaller, at times even negligible, result for the tail correction.

In Fig. 1, the corrected surface tension results as a function of temperature are plotted. The results with correction for the cylindrical truncation of 3.5  $\sigma$  are in good agreement with those of Mecke *et al.* using spherical truncation of 6.5  $\sigma$ .<sup>18</sup> The surface tension vanishes as the critical temperature is approached. Although these results show a qualitative agreement they are higher than those obtained from experimental observation of Argon.<sup>19–21</sup> This difference in results is possibly due to a significant contribution of three-body and higher-body potentials on the surface tension in real Argon as opposed to the two-body interactions of a Lennard-Jones fluid used in the present simulations. Simulations taking the effect of a three-body interaction by Lee *et al.*<sup>16</sup> are included in Fig. 1 and suggest that this is, in fact, the major source of discrepancy between the present results and experimental work.

Figure 2 shows the density profile of the system along the z-axis for a range of temperatures. The length of the

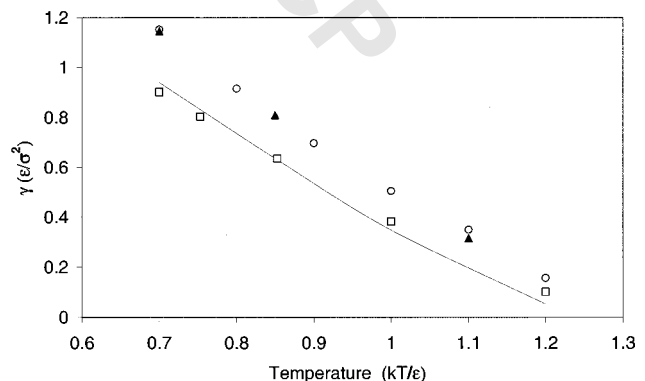


FIG. 1. Simulation results for tail-corrected planar surface tension as a function of temperature. Present work  $s_c^* = 3.5$  and  $z_c^* = 3.5$  (○), Mecke *et al.*<sup>17</sup>  $r_c^* = 6.5$  (▲), Lee *et al.*<sup>16</sup> using perturbation theory including 3-body perturbation (□), experimental results for liquid Argon (line).

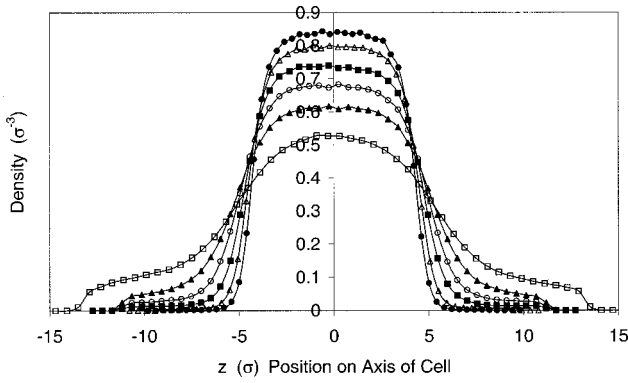


FIG. 2. Simulated planar density profile,  $\rho^*(z)$ , for cutoffs,  $z_c^* = 3.5$ ,  $s_c^* = 3.5$ .  $T^* = 0.70$  (●),  $T^* = 0.80$  (△),  $T^* = 0.90$  (■),  $T^* = 1.00$  (○),  $T^* = 1.10$  (▲),  $T^* = 1.20$  (□).

system was adjusted with increasing temperature to allow planar two-phase coexistence. This is signified by the presence of flat regions in the density profiles, which means the pressure of the system is equal to the coexistence pressure. However as the critical temperature was neared it became increasingly difficult to achieve these flat regions in the density profile, even by adjusting the volume of the system. This difficulty can be seen most prominently at the highest temperature,  $T^* = 1.20$ . As temperatures increase, a systematic decrease in the liquid density and increase in the vapor density can be seen. Also of significance is the increase in the width of the interfacial region between the liquid and vapor phases as temperature approaches the critical temperature. The sudden drop in vapor density at the ends of each profile is due to the presence of the external potential at the edge of the box.

### III. SPHERICAL GEOMETRY

#### A. Spherical truncation correction

A Lennard-Jones fluid was simulated at a liquid density close to coexistence at a temperature,  $T^*$  in a cubic box with sides of length  $L^*$ . The solvent particles interact not only with each other but also with a hard sphere cavity with radius,  $R$ , located in the center of the box. The potential due to this solute is of the form

$$u_{hs}(r_i) = \begin{cases} 0, & r_i > R \\ \infty, & r_i < R \end{cases} \quad (3.1)$$

Analogous to the planar problem the solvent-solvent interactions are subject to an inhomogeneous spherical truncation and correction technique using a cutoff radius,  $r_c < L/2$ . In terms of the pair density the total solvent-solvent potential energy is given by Eq. (2.5). Assuming the system has spherical symmetry and rotating it so that  $r_1$  lies along the  $z$ -axis, the tail contribution is

$$U_C = 4\pi^2 \int_0^\infty dr_1 \rho(r_1) r_1^2 \int_0^\infty dr_2 \rho(r_2) r_2^2 \int_{\theta_{\min}}^{\theta_{\max}} d\theta \sin \theta u(r_{12}). \quad (3.2)$$

The limits on the angular integral are given below. For each step in the Monte Carlo simulation the change in energy due

to the single trial movement of the  $i$ th atom, Eq. (2.13) is required. The spherical truncation correction due to this trial move is

$$T(r_1) = 2\pi \int_0^\infty dr_2 \rho(r_2) r_2^2 \int_{\theta_{\min}}^{\theta_{\max}} d\theta u \sin \theta u(r_{12}). \quad (3.3)$$

Using the asymptotic limit of the Lennard-Jones fluid,

$$u(r_{12}) \sim -4\epsilon \left( \frac{\sigma}{r_{12}} \right)^6,$$

and the trigonometric identity  $r_{12}^2 = r_1^2 + r_2^2 - 2r_1 r_2 \cos \theta$ , one obtains

$$T(r_1) = \frac{2\pi\epsilon\sigma^6}{r_1} \int_0^\infty dr_2 \rho(r_2) r_2 \times \left[ \frac{1}{(r_1^2 + r_2^2 - 2r_1 r_2 \cos \theta)^2} \right]_{\theta_{\min}}^{\theta_{\max}}. \quad (3.4)$$

To evaluate this equation it is necessary to know the correct values of  $\theta_{\min}$  and  $\theta_{\max}$ .

Case 1  $r_1 > r_c$

1(a)  $r_2 < r_1 - r_c$   $\theta_{\min} = 0$   $\theta_{\max} = \pi$

1(b)  $r_2 > r_1 + r_c$   $\theta_{\min} = 0$   $\theta_{\max} = \pi$

1(c)  $r_1 - r_c < r_2 < r_1 + r_c$   $\theta_{\min} = r_1^2 + r_2^2 - r_c^2 / 2r_1 r_2$   $\theta_{\max} = \pi$ .

Case 2  $r_c > r_1$

2(a)  $r_2 < r_c - r_1$   $\theta_{\min} = \theta_{\max}$

2(b)  $r_2 > r_c + r_1$   $\theta_{\min} = 0$   $\theta_{\max} = \pi$

2(c)  $r_c - r_1 < r_2 < r_c + r_1$   $\theta_{\min} = r_1^2 + r_2^2 - r_c^2 / 2r_1 r_2$   $\theta_{\max} = \pi$ .

At some distance from the center of the cavity the perturbation in the density by the solute is negligible. The integral of the density profile is dominated by the far region, and so one can define the density of the simulations as

$$\rho_{\text{bulk}} = \frac{N}{L^3 - \frac{4}{3}\pi R^3}, \quad (3.5)$$

where the denominator is the volume accessible to the atoms. If one assumes that the density has reached its bulk value by the edge of the simulation cell, Eq. (3.4) can be rewritten as

$$T(r_1) = \frac{2\pi\epsilon\sigma^6}{r_1} \int_0^L dr_2 \rho(r_2) r_2 \times \left[ \frac{1}{(r_1^2 + r_2^2 - 2r_1 r_2 \cos \theta)^2} \right]_{\theta_{\min}}^{\theta_{\max}} + \frac{2\pi\epsilon\sigma^6 \rho_{\text{bulk}}}{r_1} \int_L^\infty dr_2 r_2 \times \left[ \frac{1}{(r_1^2 + r_2^2 - 2r_1 r_2 \cos \theta)^2} \right]_{\theta_{\min}}^{\theta_{\max}}. \quad (3.6)$$

The first part of this equation is evaluated numerically during the simulation using the current average density profile. The second part may be evaluated analytically.

The change in the tail correction is included during the evaluation of the change in the potential for a trial move in the Metropolis algorithm. Further, the total truncation correc-

tion to the potential energy of the system is the sum of the individual contributions of each atom in the simulation

$$U_C = \frac{1}{2} \sum_{i=1}^N T(r_i). \quad (3.7)$$

## B. Theory

For a spherical system with radius  $S$ , with cavity of radius  $R$ ,  $dV = 4\pi S^2 dS - 4\pi R^2 dR$ . If  $dS = 0$ , the volume derivative of the Helmholtz free energy is given by

$$\frac{\partial F}{\partial V} = -\frac{kT}{Q} \frac{\partial Q}{\partial V} = -\frac{kT}{4\pi R^2 Q} \frac{\partial Q}{\partial R}, \quad (3.8)$$

where  $Q$  is the configuration integral,

$$\begin{aligned} Q &= S^{3N} \int_{R/S}^1 e^{-\beta u_{\text{LJ}}(r^N)} d\hat{r}^N \\ &= S^{3N} \prod_{i=1}^N \int_{R/S}^1 d\hat{r}_i \hat{r}_i^2 \int dw_i e^{-\beta u_{\text{LJ}}(r^N)}. \end{aligned} \quad (3.9)$$

where  $dw_i = \sin \theta_i d\theta_i d\phi_i$  and  $\hat{r} = \vec{r}/S$ .

The derivative is

$$\begin{aligned} \frac{\partial Q}{\partial R} &= S^{3N} \sum_{i=1}^N \int_{R/S}^1 d\hat{r}_1 \hat{r}_1^2 \dots d\hat{r}_{j-1} \hat{r}_{j-1}^2 \int dw^{j-1} \left( -\frac{4\pi R^2}{S} \frac{\partial}{\partial R} \right) \\ &\quad \times \int_{R/S}^1 d\hat{r}_{j+1} \hat{r}_{j+1}^2 \dots d\hat{r}_N \hat{r}_N^2 \int dw^{N-j} e^{-\beta u_{\text{LJ}}(r^N)} \Big|_{\hat{r}_j=R/S} \\ &= \frac{-4\pi S^{3N} R^2 N}{S^3} \int_{R/S}^1 d\hat{r}_2 \hat{r}_2^2 \dots d\hat{r}_N \hat{r}_N^2 \\ &\quad \times \int dw^{N-1} e^{-\beta u_{\text{LJ}}(r^N)} \Big|_{\hat{r}_1=R/S}. \end{aligned} \quad (3.10)$$

The contact density can be expressed as

$$\rho_c = \left\langle \sum_{i=1}^N \delta(R - r_i) \right\rangle. \quad (3.11)$$

The angular brackets denote the ensemble average, and hence one has

$$\begin{aligned} \rho_c &= \frac{1}{Q} \int_R^S e^{-\beta u_{\text{LJ}}(r^N)} dr^N \sum_{i=1}^N \delta(R - r_i) \\ &= \frac{N}{Q} \int_R^S dr_2 \dots dr_N e^{-\beta u_{\text{LJ}}(r^N)} \Big|_{r_1=R}. \end{aligned} \quad (3.12)$$

Substituting Eq. (3.12) into Eq. (3.10) yields a relationship between the contact density and the derivative of the Helmholtz free energy,<sup>15</sup>

$$\frac{\partial F(R)}{\partial R} = 4\pi R^2 kT \rho_c. \quad (3.13)$$

Furthermore for a canonical system  $F(R)$  is related to the curvature dependent surface tension,  $\gamma(R)$ , by<sup>2,4,11,14</sup>

$$F(R) = Vp + A\gamma(R), \quad (3.14)$$

where  $A$  and  $V$  are the surface area and volume of the cavity, respectively, and  $p$  is the pressure of the liquid far from the cavity. In this work  $R$  has been chosen to be the physical radius of the cavity, as this is the simplest and most obvious value with which to work. It would have been equally valid to specify  $R$  as some other arbitrarily chosen radius, such as the equimolar radius or the radius of the surface of tension, if these exist. This equation defines  $\gamma(R)$  for the present choice of  $R$ . The right hand side of Eq. (3.13) can be obtained from the simulation using Eq. (3.11), and hence  $\gamma(R)$  follows by numerical integration.

Another relationship, derived by Henderson,<sup>14</sup> relates the curvature dependent surface tension of a fluid surrounding a hard wall cavity to the derivative of the contact density with respect to the radius of the cavity,

$$\gamma(R) = \frac{-kTR^2}{2} \frac{\partial \rho_c(R)}{\partial R}. \quad (3.15)$$

This expression is only valid in the large radius limit.

The surface tension can also be obtained as an integral over the pressure tensor, although there is some uncertainty on the microscopic expression for the latter.<sup>2,6,13,14</sup> This approach has not been used here.

## C. Small cavity theory

For small cavities,  $R < \approx \sigma$ , an asymptotic expansion can provide a useful check on the accuracy of contact density measurements. Following the arguments of scaled particle theory,<sup>22</sup> in this regime small cavities can interact with only one solvent particle at any one time. An insertion of a cavity into a system would be forbidden if the cavity center is within  $R$  of an atom center. The forbidden volume is given by

$$V_f = N \frac{4}{3} \pi R^3. \quad (3.16)$$

This assumes that the forbidden volume about each atom do not overlap, which will be true for small enough cavities. The probability of a successful insertion of a cavity with radius  $R$  is

$$P(R) = 1 - \frac{V_f}{V} = 1 - \rho_{\text{bulk}} \frac{4}{3} \pi R^3. \quad (3.17)$$

Since the probability of inserting a cavity,  $R=0$ , is  $P(R=0) = 1$ , and since the probability is proportional to the Boltzmann factor of the Helmholtz free energy,

$$P(R) = e^{-\beta F(R)}, \quad (3.18)$$

one has

$$F(R) = -kT \ln \left( 1 - \rho_{\text{bulk}} \frac{4}{3} \pi R^3 \right). \quad (3.19)$$

Equation (3.19) with Eq. (3.14) gives the curvature dependent surface tension directly in the small radius limit. The derivative of Eq. (3.19) is

$$\frac{\partial F(R)}{\partial R} = \frac{kT \rho_{\text{bulk}} 4\pi R^3}{1 - \rho_{\text{bulk}} \frac{4}{3} \pi R^3}. \quad (3.20)$$

By substituting Eq (3.13) into Eq. (3.8) a small cavity expansion for the contact density theory is derived

$$\rho_c = \frac{\rho_{\text{bulk}}}{1 - \rho_{\text{bulk}} \frac{4}{3} \pi R^3}, \quad (3.21)$$

This expression is exact in the limit  $R \rightarrow 0$ , and is expected to be a good approximation for  $R < \approx \sigma$ .

Small cavity theory can also be extended to an analysis of the solute-solvent radial distribution function,  $g_{01}$ ,

$$g_{01}(\vec{r}, \vec{s}) = \frac{V^2}{Q(N, R)} \int d\mathbf{r}_0 d\mathbf{r}_1^N e^{-\beta U_{\text{LJ}}} e^{-\beta U_{hs}} \times \delta(\vec{r}_0 - \vec{r}) \delta(\vec{r}_1 - \vec{s}), \quad (3.22)$$

where  $Q(N, R)$  is the configuration integral for a system of  $N$  atoms with a cavity radius of radius  $R$ . If  $R < |\vec{r} - \vec{s}| < \sigma - R$ , then  $U_{hs} = 0$  and this becomes

$$g_{01}(r, s) = \frac{V^2 \int d\mathbf{r}^{N-1} e^{-\beta U_{\text{LJ}}|_{r_N=s}}}{(V - \frac{4}{3} \pi R^3)^N \int d\mathbf{r}^N e^{-\beta U_{\text{LJ}}}}. \quad (3.23)$$

Since the integrals are independent of  $R$ , due to homogeneity the one in the denominator is  $V$  times the one in the numerator, and one obtains

$$g_{01}(r, s) = \frac{V}{V - \frac{4}{3} \pi R^3 N} = \frac{1}{1 - \frac{4}{3} \pi R^3 \rho_{\text{bulk}}}, \quad (3.24)$$

which is independent of  $|\vec{r} - \vec{s}|$ . This result is valid for solvent atoms within about a solvent diameter of a small cavity. The solvent density profile about the solute is

$$\rho(r) = \rho_{\text{bulk}} g_{01}(|\vec{r} - \vec{s}|). \quad (3.25)$$

#### D. Simulation

The local density,  $\rho(r_i)$ , in the simulation was measured as the average number of particles,  $\bar{h}(i)$ , in a spherical shell of width  $\Delta_r$  around the radius  $r_i$  divided by the volume of the shell

$$\rho(r_i) = \frac{\bar{h}(i)}{\frac{4}{3} \pi \left[ \left( r_i + \frac{\Delta_r}{2} \right)^3 - \left( r_i - \frac{\Delta_r}{2} \right)^3 \right]}, \quad (3.26)$$

where  $r_i = R + (i-1)\Delta_r + \Delta_r/2$ .

The contact density,  $\rho_c$ , was calculated by linear extrapolation of the local density measurements from the first two shells

$$\rho_c = \rho(r_1) + \frac{(\rho(r_1) - \rho(r_2))}{2}. \quad (3.27)$$

A problem arises in the calculation of the local density in the first few shells directly surrounding a small cavity. At the bulk densities dealt with in this paper the average number of atoms in these cell can be very small. For example, for a system with  $\rho_{\text{bulk}}^* = 0.84$ ,  $R^* = 0.2$ ,  $\Delta_r^* = 0.1$  and assuming  $\rho^*(r_1) = \rho_{\text{bulk}}^*$ , the average number of atoms in the first two shells would be  $\bar{h}(1) = 0.07$  and  $\bar{h}(2) = 0.13$ . Measurements of densities at these small radii become highly dependent on the movements of a very small number of atoms into and out

of the volume element, which increases the statistical fluctuations in the results. In contrast, due to the larger volume element, many more atoms contribute to measurements made further from the surface of the cavity. Since accurate values of the contact density are required, to overcome this problem a preferential sampling scheme was implemented.<sup>23,24</sup> Here, after each complete cycle of trial moves, every particle within the *vicinal* radius,  $r_v$ , from the center of the cavity was identified and then moved and sampled up to a further 60 times. During this further period of sampling, in order to preserve microscopic reversibility, any trial movement moving an atom beyond the vicinal radius was immediately rejected. This vicinal sampling significantly reduced fluctuations in the density profile and increased the accuracy of the measured contact density.

Simulations were run for three temperatures  $T^* = 0.70$ , 1.00, and 1.20 at the constant coexistence liquid bulk densities measured in the planar section of this study,  $\rho_{\text{bulk}}^* = 0.84$ , 0.68, and 0.53 respectively. The size of the simulation cell and the number of atoms within it were increased with increasing cavity size but the bulk density, defined by Eq. (3.5) was kept constant at all times. A constraint was placed on the minimum length of the box,  $L^*/2 - R^* > 3.5$ , so as to minimize any interaction between the cavity and its periodic images.

By increasing the size of the simulation cell and the number of atoms and keeping the overall density, Eq. (3.5), constant as the size of the cavity is increased, constant chemical potential conditions can be maintained to a good approximation. This canonical Monte Carlo simulation method represents an economic alternative to constant chemical potential simulations. A similar constraint was used in simulations by Stecki and Toxvaerd.<sup>11</sup> They kept the average density outside a radius  $r^* = R^* + 1.666$  constant, whereas here the density outside  $R^*$  was kept constant. Here it was found that the local density at the edge of the simulation approached the value of the bulk density and the adsorption excess due to the cavity gave a negligible contribution. To confirm this, measurements of the contact density were made for the same cavity in two different sized systems, with the same overall density. This produced the same result within standard error. It was concluded that keeping the bulk density constant, as described above, was an acceptable method. Another alternative to constant chemical potential simulations would have been to use constant pressure simulations. Such an isobaric approach could be implemented using expressions for the pressure tensor given in the literature.<sup>2,6,13,14</sup>

From an initial setup, 20 000 cycles were taken to equilibrate the system. Statistical measurements were made in the following 75 000 cycles. Furthermore, at the completion of each cycle, there was a further 60 vicinal cycles. The vicinal radius was,  $r_v^* = R^* + 1.2$  for  $R^* < 1.5$ . For  $R^* > 1.5$ , no vicinal sampling was required.

#### E. Results

The results for the density profiles are shown in Fig. 3 and Fig. 4, for  $T^* = 0.70$  and 1.00, respectively, for three

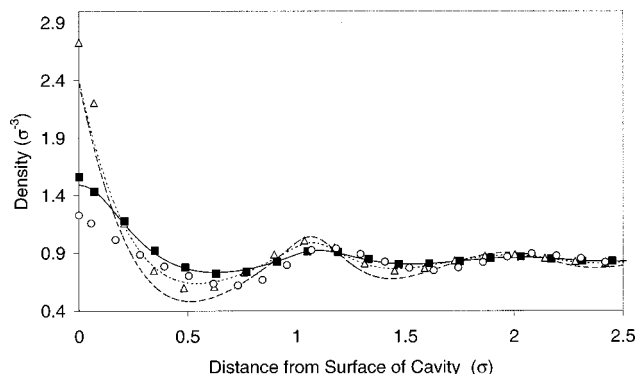


FIG. 3. Density profiles about a spherical cavity,  $T^*=0.70$ . Monte Carlo  $R^*=0.5$  (■), Percus–Yevick  $R^*=0.5$  (full line), MC  $R^*=0.9$  (△), PY  $R^*=0.9$  (dotted line), MC  $R^*=3.1$  (○), PY  $R^*=3.1$  (dashed line).

examples of increasing cavity size. In general the contact density is higher than the bulk density. The density drops as the distance from the edge of the cavity is increased and a subsequent damped oscillation around the bulk density value is observed. These results are compared with those obtained by using the Percus–Yevick integral equation technique. The Percus–Yevick technique was found to give an excellent agreement for Monte Carlo simulations of systems for small cavities. However, as the cavity size was increased, the integral equation method begins to fail close to the solute. The overestimation of the contact density for large cavities is consistent with the fact that Percus–Yevick gives a larger solvent pressure than the simulated coexistence pressure (see the following). The density profile of the largest cavity in Fig. 4 is of particular interest as densities at all distances close to the solute are smaller than the bulk density. Instead of an oscillation around the bulk density a monotonic increase was observed until it reaches this value.

Figures 5 and 6 compare the results of the simulation with Percus–Yevick and small cavity theory for two temperatures. The results show that small cavity theory provides an accurate estimation of the solute–solvent radial distribution function close to the surface of the small cavity. The distance from the surface of the cavity, over which the small cavity theory remains an accurate approximation, appears to be dependent upon the size of the cavity. The small cavity

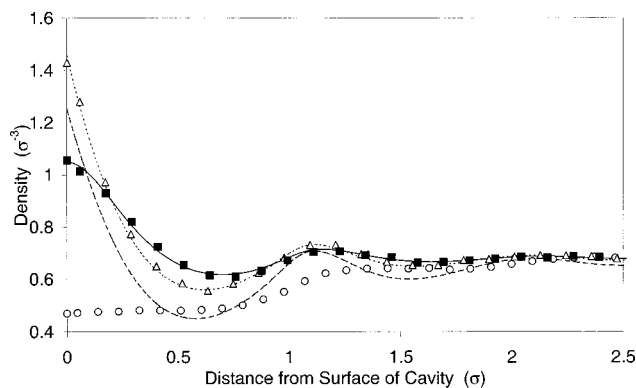


FIG. 4. Density profiles about a spherical cavity,  $T^*=1.00$ , symbols and lines as in preceding Fig. 3, except that the largest radius is  $R^*=3.0$ .

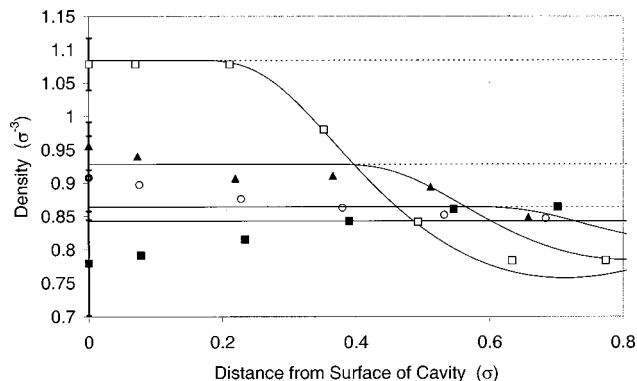


FIG. 5. Density profiles close to the surface of small cavities. MC (symbols), PY (full line) and Small Cavity Theory (dashed line),  $T^*=0.70$ . The cavity radius is  $R^*=0.1$  (■),  $R^*=0.2$  (○),  $R^*=0.3$  (▲),  $R^*=0.4$  (□).

theory remains accurate for a cavity with  $R^*=0.1$  over a radius of  $r^*-R^*\approx 0.9$  while for a larger cavity,  $R^*=0.5$ , it is accurate over a smaller span,  $r^*-R^*\approx 0.2$ .

The adsorption excess per unit area,  $\Gamma(R)$ , can be calculated from the individual density profiles as we systematically increase the cavity radius,

$$\Gamma(R) = \frac{1}{R^2} \int_R^\infty dr r^2 (\rho(r) - \rho_\infty), \quad (3.28)$$

where  $\rho_\infty$  is the density far from the surface of the cavity.  $\rho_\infty$  was calculated as the average density in the region  $r^*=L^*-2$  to  $r^*=L^*$ . The estimated  $\Gamma(R)$ , for each of the three temperatures, is presented in Fig. 7. There was a large error in measurements made at very small values of  $R$ . For increasing cavity size we find that the adsorption excess becomes negative, as would be expected. At a higher temperature,  $\Gamma(R)$  tends to a negative value more quickly. The inset of Fig. 7 shows a comparison of  $\rho_{\text{bulk}}^*$  [Eq. (3.5)] and  $\rho_\infty$ . A slight increase in  $\rho_\infty$  from the bulk density can be seen for  $T^*=1.00$  and  $1.20$  at large  $R$ . The density of the liquid surrounding the cavity is significantly less than  $\rho_{\text{bulk}}^*$  for these temperature at larger radii (see Fig. 4), an effect not seen at these radii for  $T^*=0.70$ . This is possibly the cause of the slightly higher density at the edge of the simulation cell. However this discrepancy in densities is minimal and further

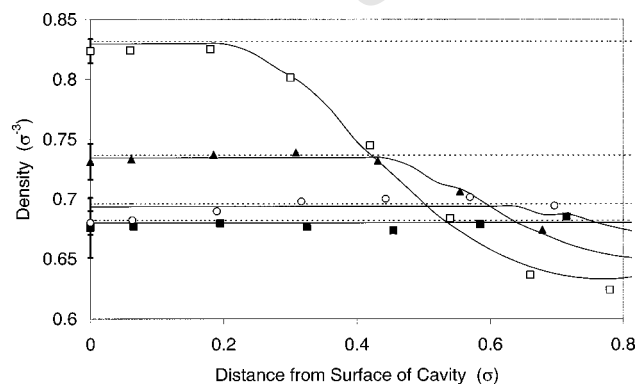


FIG. 6. Density profiles close to the surface of small cavities,  $T^*=1.00$ . Symbols and lines as in Fig. 5.

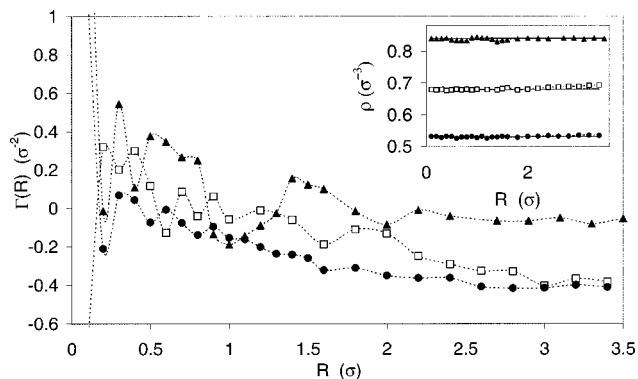


FIG. 7. The adsorption excess per unit area,  $\Gamma(R)^*$ .  $T^*=0.70$  (▲),  $T^*=1.00$  (□),  $T^*=1.20$  (●). Inset. Density far from the cavity,  $\rho_c^*$ ,  $T^*=0.70$  (▲),  $T^*=1.00$  (□),  $T^*=1.20$  (●),  $\rho_{\text{bulk}}$ , Eq. (3.5) (horizontal line).

validates the decision to keep Eq. (3.5) constant as an alternative to a constant chemical potential simulation.

The simulation results for the contact densities at each temperature are shown in Fig. 8 and these are used to test the Percus–Yevick results and the small cavity theory predictions. For small cavities all results are in good agreement. Small cavity theory breaks down quickly after  $R^* \approx 0.5–0.6$  and diverges. In general the singlet Percus–Yevick becomes increasingly inaccurate as the solute size is increased. For the case of a hard-sphere fluid, the singlet Percus–Yevick underestimates the contact density at the surface of large solutes and planar walls.<sup>25</sup> For the present Lennard-Jones fluid, the singlet Percus–Yevick evidently overestimates the contact density.

Figure 8 also shows a polynomial fit of the simulated contact density values for  $R > 1.2 \sigma$ ,

$$\rho_c(R) = a_0 + \frac{a_1}{R} + \frac{a_2}{R^2}. \quad (3.29)$$

The reason for only using three coefficient terms in this expansion is that Eq. (3.15) is not guaranteed exact beyond this order. This equation allows one to predict the planar wall value of the contact density, i.e.,  $\rho_c(R \rightarrow \infty) = a_0$ . This is a useful result as the planar limit of the contact density can be used to calculate the pressure of the liquid,

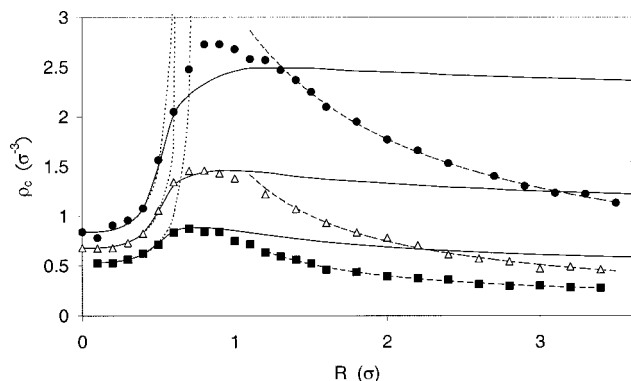


FIG. 8. Contact density,  $\rho_c^*$  as a function of cavity radius,  $R^*$ , Monte Carlo (symbols), Percus–Yevick (full line), Small Cavity Theory (dotted line), least squares polynomial fit for  $R^* > 1.2$  (dashed line).  $T^*=0.70$  (●),  $T^*=1.00$  (Δ),  $T^*=1.20$  (■).

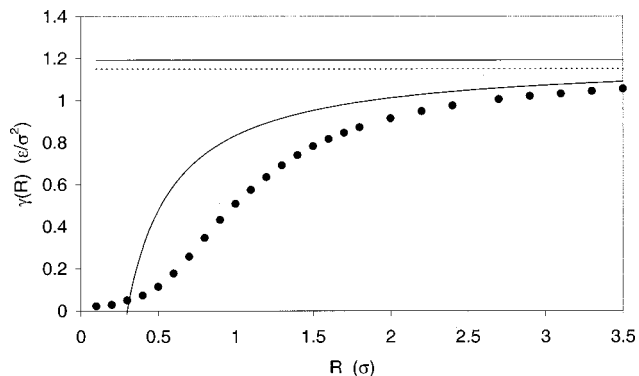


FIG. 9. Curvature dependent surface tension,  $\gamma(R)^*$ ,  $T^*=0.70$ , calculated using Eq. (3.14) (●), and Eq. (3.15) (line). The planar liquid-vapor interface surface tension value (dashed horizontal line) (see Table I). The planar surface tension value from Eq. (3.32) (horizontal line).

$$p = \rho(R = \infty)kT. \quad (3.30)$$

By substituting the derivative of Eq. (3.29) into Eq. (3.15) and equating with Eq. (1.1), one obtains,

$$\gamma \left( 1 - \frac{2\delta}{R} \right) = \frac{kTa_1}{2} + \frac{kTa_2}{R}. \quad (3.31)$$

The planar surface tension predicted by Eq. (3.15) may be evaluated directly from the parameter  $a_1$ , from the polynomial fit of the contact density,

$$\gamma_\infty = \frac{kTa_1}{2}. \quad (3.32)$$

Similarly the Tolman length may be expressed as

$$\delta = -\frac{kTa_2}{2\gamma_\infty} = -\frac{a_2}{a_1}. \quad (3.33)$$

Using the polynomial fit to the contact density, Tolman's expression for the curvature dependent surface tension, Eq. (3.31), is plotted in Figs. 9–11. The planar surface tension estimates obtained using Eq. (3.32) are also shown, as horizontal lines, and compared to the results of the simulated planar liquid-vapor interface given in Table I. The Tolman lengths calculated from Eq. (3.33) are given in Table II.

Alternatively, using the fact that the contact density is the derivative of the Helmholtz free energy, curvature depen-

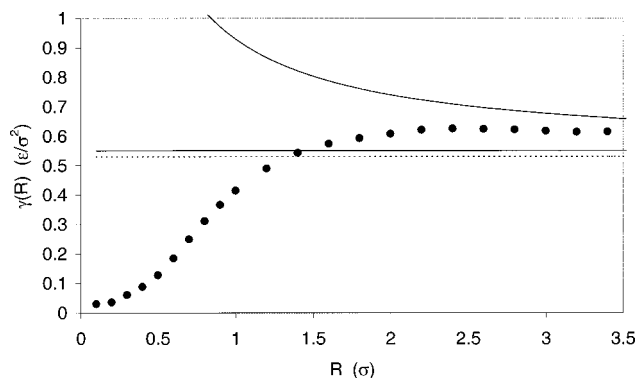


FIG. 10. Curvature dependent surface tension,  $\gamma(R)^*$ ,  $T^*=1.00$ , symbols and lines as in Fig. 9.

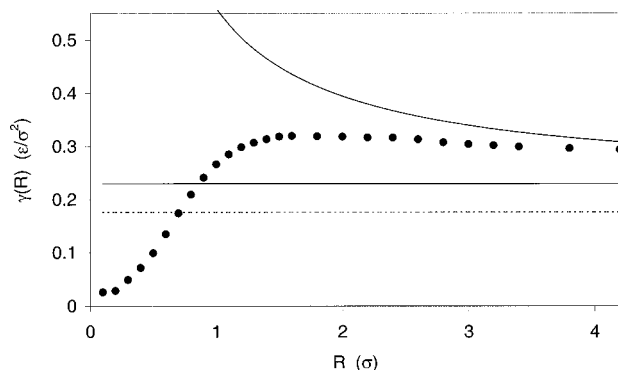


FIG. 11. Curvature Dependent Surface Tension,  $\gamma(R)^*$ ,  $T^*=1.20$ , symbols and lines as in Fig. 9.

dent surface tension can be obtained exactly for all radii. Equation (3.13) may be numerically integrated to give the Helmholtz free energy,  $F(R)$ . Subtraction of the pressure term from  $F(R)$  in Eq. (3.14) gives the curvature dependent surface tension. In the hard-sphere cavity simulations, however, the pressure was not calculated. The simulations were performed as a liquid under conditions close to liquid–vapor coexistence, therefore, it was expected that the pressure of this system would be close to that measured for the liquid–vapor interface. Substituting this coexistence pressure,  $p_{\text{coex}}$ , into Eq. (3.14),  $\gamma(R)$  reached the planar value of the surface tension,  $\gamma_\infty$ , but continues to increase significantly in all cases. This effect implies that the pressure in the hard-sphere cavity simulations is larger than the coexistence pressure. The pressure, close to the coexistence values used in the simulations, is highly dependent on the density of the system. A small departure from the planar coexistence liquid density, (e.g., ignoring the effects of the adsorption deficit due to the cavity) can result in a relatively large increase in the pressure. A new pressure,  $p_{\text{fit}}$ , was chosen such that the form of  $\gamma(R)$ , calculated from Eq. (3.14), maximized its convergence to that calculated from Eq. (3.15), as can be seen in Figs. 9–11. The value of  $p_{\text{fit}}$  and the implied error in density, calculated using an equation of state<sup>26</sup> for this deviation from  $p_{\text{coex}}$ , are given in Table II. This error in the density is very small and comparable to that in the inset of Fig. 7. This value of  $p_{\text{fit}}$  was used to fix  $a_0$  in the polynomial fit

TABLE II. The measured liquid–vapor coexistence pressure,  $p_{\text{coex}}$ , is shown in comparison to the fitted pressure  $p_{\text{fit}}$ . The bulk density of the liquid,  $\rho_{\text{bulk}}$ , given by Eq. (3.5) is given for each temperature, as is the planar contact density value,  $\rho_c(\infty)$ , and the error in density implied by the difference between  $p_{\text{fit}}$  and  $p_{\text{coex}}$ ,  $\Delta\rho$ . The planar hard wall surface tension and the Tolman length calculated by Eq. (3.32) and Eq. (3.33), respectively, are also given.

$T^*$	0.70	1.00	1.20
$p_{\text{coex}}^*$	0.005	0.025	0.069
$p_{\text{fit}}^*$	0.210	0.100	0.138
$\rho_{\text{bulk}}^*$	0.84	0.68	0.53
$\rho_c(\infty)^*$	0.15	0.10	0.14
$\Delta\rho^*$	0.01	0.01	0.04
$\gamma_\infty^*$	1.19	0.551	0.229
$\delta^*$	0.15	−0.34	−0.72

to the contact density, Eq. (3.29). This had a minimal effect on the planar surface tension and the curvature dependent surface tension. However, the Tolman length itself was very sensitive to changes in the fit.

#### IV. DISCUSSION

The main focus of this paper was to examine the behavior of the surface tension of a liquid close to coexistence surrounding a small cavity. The contact density profile was used by two separate means to evaluate the surface tension. The large cavity density expansion, Eq. (3.15), provided not only a measure of the curvature dependent surface tension, but also an estimate of the planar surface tension, Eq. (3.32) and the Tolman length, Eq. (3.33). The planar hard wall surface tension from this method, shown in Figs. 9–11, can be seen to be close to the planar liquid–vapor interface results, measured in Sec. II. This is a highly encouraging result and implies that the hard-sphere cavity simulations provide a viable simpler alternative to the simulation of small bubbles when investigating the size dependence of surface tension.

The least squares polynomial fit of the contact density is of some concern. We have used a three term polynomial expansion; it is possible but not guaranteed that an extra  $a^3/R^3$  term would remain valid and improve the fit. The regime of validity of Eq. (3.15) is unknown, and it is therefore unclear if a better fit at smaller cavity radii would be more meaningful. The curvature dependent and planar surface tension results are relatively insensitive to the number of terms used in the fit. However, the Tolman length is very sensitive to the number of terms and the fitting regime.

While it is unfortunate that an independent measure of the pressure in the hard-sphere cavity simulations could not be made, we believe that  $p_{\text{fit}}$  is an accurate representation of this value. From the Helmholtz free energy route to the surface tension it can be seen that at very small radii  $\gamma(R)$  is much smaller than its planar value. The two methods of obtaining surface tension can be seen converging to each other in the simulated cavity regimes shown in Figs. 9–11. It is of some concern that the results of Eq. (3.15) do not have qualitative agreement with the Helmholtz route even at the larger radii. The fact that they tend toward each other but are not in full agreement in Figs. 9–11 implies that the regime of quantitative applicability of Tolman’s expression is beyond even these large cavities.

Due to the sensitivity of the Tolman length measurement on the form of the polynomial fit to the contact density, it is suggested that the results of the calculation of  $\delta$ , be taken as a guide to its size but not as an exact result. There is evidence, however, that the Tolman length becomes more negative as the temperature approaches the critical temperature, as was found in Ref. 27. In the Helmholtz route, for  $T^*=1.00$  and 1.20, any reasonable value of  $p_{\text{fit}}$  will cause  $\gamma(R)$  to become greater than  $\gamma_\infty$ , at suitably large radii. A negative Tolman length value is therefore required to achieve the correct asymptotic limit. In contrast, for  $T^*=0.70$ ,  $\gamma(R)$  appears to approach  $\gamma_\infty$  from below, which implies a positive Tolman length. These results are consistent with the large radius expansion of the contact density results and the Tolman length results given in Table II.

These conclusions are based on the surface energy of a cavity. While we have presented evidence that this is a good model for the planar liquid-vapor interface (cf.  $\gamma_\infty = \gamma_{lv}$ ), it requires an additional assumption to apply the model to non-zero curvatures. This question requires further research as does the question as to whether the Tolman length of a bubble is the same as that of a droplet.<sup>28</sup>

<sup>1</sup>R. C. Tolman, J. Chem. Phys. **17**, 333 (1949).

<sup>2</sup>J. Rowlinson and B. Widom, *Molecular Theory of Capillarity* (Clarendon, Oxford, 1982).

<sup>3</sup>C. Fradin, A. Brasiau, D. Smilgies, M. Alba, N. Boudet, K. Mecke, and J. Daillant, Nature (London) **403**, 871 (2000).

<sup>4</sup>M. J. P. Nijmeijer, C. Bruin, A. B. van Woerkom, A. F. Bakker, and J. M. J. van Leeuwen, J. Chem. Phys. **96**, 565 (1992).

<sup>5</sup>M. J. Haye and C. Bruin, J. Chem. Phys. **100**, 556 (1994).

<sup>6</sup>H. El Bardouni, M. Mareschal, R. Lovett, and M. Baus, J. Chem. Phys. **113**, 9804 (2000).

<sup>7</sup>E. M. Blokhuis and D. Bedeaux, J. Chem. Phys. **97**, 3576 (1992).

<sup>8</sup>E. van Giessen, E. M. Blokhuis, and D. J. Bukman, J. Chem. Phys. **108**, 1148 (1998).

<sup>9</sup>V. I. Kalikmanov, Phys. Rev. E **55**, 3068 (1997).

<sup>10</sup>T. V. Bykov and X. C. Zeng, J. Chem. Phys. **111**, 3705 (1999).

<sup>11</sup>J. Stecki and S. Toxvaerd, J. Chem. Phys. **93**, 7342 (1990).

<sup>12</sup>A. Samborski, J. Stecki, and A. Poniewierski, J. Chem. Phys. **98**, 8958 (1992).

<sup>13</sup>A. Poniewierski and J. Stecki, J. Chem. Phys. **106**, 3358 (1997).

<sup>14</sup>J. R. Henderson, Mol. Phys. **50**, 741 (1983).

<sup>15</sup>J. R. Henderson, *Fluid Interfacial Phenomena*, edited by C. A. Croxton (Wiley, New York, 1986).

<sup>16</sup>J. K. Lee, J. A. Barker, and G. M. Pound, J. Chem. Phys. **60**, 1976 (1974).

<sup>17</sup>D. R. Berard, P. Attard, and G. N. Patey, J. Chem. Phys. **98**, 7236 (1993).

<sup>18</sup>M. Mecke, J. Winkelmann, and J. Fischer, J. Chem. Phys. **107**, 9264 (1997).

<sup>19</sup>F. B. Sprow and J. M. Prausnitz, Trans. Faraday Soc. **62**, 1097 (1966).

<sup>20</sup>D. Stansfield, Proc. Phys. Soc. London **72**, 854 (1958).

<sup>21</sup>K. C. Nadler, J. A. Zollweg, W. B. Steett, and I. A. McLure, J. Colloid Interface Sci. **122**, 530 (1987).

<sup>22</sup>H. Reiss and H. L. Frisch, J. Chem. Phys. **31**, 369 (1959).

<sup>23</sup>J. C. Owicki and H. A. Scheraga, Chem. Phys. Lett. **47**, 600 (1977).

<sup>24</sup>P. Attard, J. Chem. Phys. **98**, 2225 (1993).

<sup>25</sup>P. Attard, J. Chem. Phys. **91**, 3083 (1989).

<sup>26</sup>K. Johnson, J. A. Zollweg, and K. E. Gubbins, Mol. Phys. **78**, 591 (1993).

<sup>27</sup>L. Granasy, J. Chem. Phys. **109**, 9660 (1998).

<sup>28</sup>R. Guermeur, F. Biquard, and C. Jacolin, J. Chem. Phys. **82**, 2040 (1985).